Multimodal neuroimaging dissociates hemodynamic and electrophysiological correlates of error processing

Yigal Agam[a,b], Matti S. Hämäläinen[b,c], Adrian K. C. Lee[b,c], Kara A. Dyckman[a,b], Jesse S. Friedman[a,b,1], Marlisa Isom[a,b], Nikos Makris[a,b,d], and Dara S. Manoach[a,b,2]

Departments of [a]Psychiatry, [c]Radiology, and [d]Neurology, Massachusetts General Hospital, Harvard Medical School, Boston, MA 02215; and [b]Athinoula A. Martinos Center for Biomedical Imaging, Charlestown, MA 02129

Edited by Edward E. Smith, Columbia University, New York, NY, and approved September 9, 2011 (received for review March 3, 2011)

Recognizing errors and adjusting responses are fundamental to adaptive behavior. The error-related negativity (ERN) and error-related functional MRI (fMRI) activation of the dorsal anterior cingulate cortex (dACC) index these processes and are thought to reflect the same neural mechanism. In the present study, we evaluated this hypothesis. Although errors elicited robust dACC activation using fMRI, combined electroencephalography and magnetoencephalography data localized the ERN to the posterior cingulate cortex (PCC). ERN amplitude correlated with fMRI activation in both the PCC and dACC, and these two regions showed coordinated activity based on functional connectivity MRI. Finally, increased microstructural integrity of the posterior cingulum bundle, as measured by diffusion tensor imaging, predicted faster error correction. These findings suggest that the PCC generates the ERN and communicates with the dACC to subserve error processing. They challenge current models that view fMRI activation of the dACC as the hemodynamic reflection of the ERN.

multimodal imaging | error processing | response monitoring | action monitoring | medial frontal cortex

Understanding the nature of brain mechanisms that flexibly modify behavior in response to its outcome is a basic goal of neuroscience. Errors provide critical information for adjusting behavior to optimize outcomes. Neuroimaging studies have identified two highly reliable neural correlates of errors: the error-related negativity (ERN), an event-related potential that peaks ∼100 ms following an error, and functional MRI (fMRI) activation of the dorsal anterior cingulate cortex (dACC) for erroneous compared with correct responses (1). Both electroencephalography (EEG) and magnetoencephalography (MEG) (2) studies of the ERN have reported a source in the dACC (a list of studies is presented in Table S1), which is consistent with models that attribute these error markers to a common underlying mechanism (1, 3, 4). The primary goal of the present study was to evaluate the hypothesis of a common mechanism by determining whether the ERN is generated by the dACC region that shows error-related fMRI activation.

The ERN has been extensively characterized. Its amplitude is greater when accuracy is emphasized over speed (5), when errors are corrected (6), and when errors incur greater loss (7). Larger ERNs are associated with lower error rates (3) and greater posterror slowing of responses (8). ERN latency predicts the speed of self-corrections (9). These findings suggest that the ERN is sensitive to the value of outcomes and mediates dynamic performance adjustments. Like the ERN, greater error-related fMRI activation of the dACC is associated with fewer errors (10, 11) and increased posterror slowing (12–14).

Although error-related dACC activation is the putative hemodynamic reflection of the ERN (1, 4), these error markers have largely been studied separately using different samples and paradigms. The few studies that have directly investigated their relationship report correlations of fMRI activation of the ACC with the ERN and/or the error waveform or response-locked electrophysiological activity (8, 15, 16) but have not estimated the source of the ERN and compared its location with that of the fMRI activation. Conversely, prior ERN source localization studies have not acquired fMRI data for comparison. When compared across studies (Fig. 1), the ERN source loci from previous studies show considerable variation in location, and although the mean falls in the dACC, all are posterior to the mean location of error-related fMRI activation [based on a metaanalysis (4)]. In addition, several sources fall in the posterior cingulate cortex (PCC) according to standard anatomical definitions that place the ACC/PCC border between $y = -2$ mm and $y = -12$ mm in Talairach space (17). The PCC is also a plausible generator of the ERN. It has shown error-related activation in several prior fMRI studies (18–20) but not nearly as consistently as the dACC, and like the ERN, its activity is modulated by the value of behavioral outcomes (21–23). A recent MEG study reported a PCC source for the feedback-related negativity, which is thought to be generated by the same generic mechanism as the ERN (24). These findings led us to question whether the ERN and error-related dACC fMRI activation reflect the same mechanism and to propose instead that they are distinct neural responses to errors.

To determine whether the ERN is generated by the same dACC region that shows error-related fMRI activation, participants performed an antisaccade task (Fig. S1) during fMRI and combined EEG and MEG. Antisaccades require one to inhibit the prepotent response of looking toward a suddenly appearing stimulus and to look instead in the opposite direction. Antisaccade errors (i.e., looking toward the stimulus) reliably elicit both dACC activation (14, 25) and the ERN (26–29). We estimated the source of the ERN from the combined EEG and MEG data. We also correlated ERN amplitude with error-related fMRI activation and examined the functional connectivity of the dACC and PCC based on fMRI data. Finally, we used diffusion tensor imaging (DTI) to determine whether the microstructural integrity of the cingulum bundle predicted the speed of corrective behavior.

Results

Behavioral Performance. The mean antisaccade error rates were 16 ± 10% and 18 ± 10% for fMRI and EEG/MEG, respectively. Errors had significantly shorter latencies than correct trials [170 ± 36 ms vs. 261 ± 41 ms; $F(1,29) = 474.50$, $P < 10^{-10}$], and although significant in both modalities, this effect showed a trend to be stronger in fMRI [modality by trial type: $F(1,29) = 3.86$, $P = 0.06$]. There was significant posterror slowing [10 ± 17 ms; $F(1,29) = 10.2$, $P = 0.003$] that did not differ by modality [$F(1,29) = 0.005$, $P = 0.94$]. A total of 98 ± 3% of errors were self-corrected in fMRI, and 96 ± 4% were self-corrected in EEG/MEG.

Author contributions: Y.A., A.K.C.L., K.A.D., and D.S.M. designed research; Y.A., A.K.C.L., K.A.D., J.S.F., M.I., and D.S.M. performed research; Y.A., M.S.H., A.K.C.L., J.S.F., M.I., N.M., and D.S.M. analyzed data; and Y.A., M.S.H., and D.S.M. wrote the paper.

The authors declare no conflict of interest.

This article is a PNAS Direct Submission.

[1]Deceased July 17, 2010.

[2]To whom correspondence should be addressed. E-mail: dara@nmr.mgh.harvard.edu.

This article contains supporting information online at www.pnas.org/lookup/suppl/doi:10.1073/pnas.1103475108/-/DCSupplemental.

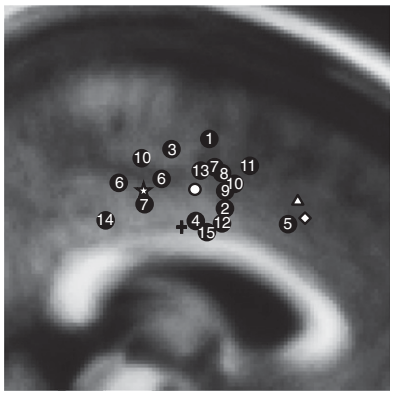

Fig. 1. A schematic summary of ERN source localizations and error-related fMRI activation displayed on a sagittal slice of the MNI305 brain at $x = 3$ mm. The numbered circles denote one or more source locations from the 15 studies (Table S1) that either provided coordinates or from which coordinates could be estimated based on anatomical landmarks. The white circle denotes the mean y and z coordinates of the ERN source studies. The triangle indicates the mean y and z coordinates of error-related fMRI activation based on a metaanalysis of 13 fMRI studies (4). The diamond indicates the peak location of error-related fMRI activation from the current study, and the star denotes the peak location of the ERN source estimate of the current study. The plus sign indicates the y coordinate ($y = -4$) of the dACC-PCC boundary, as defined by Desikan et al. (54).

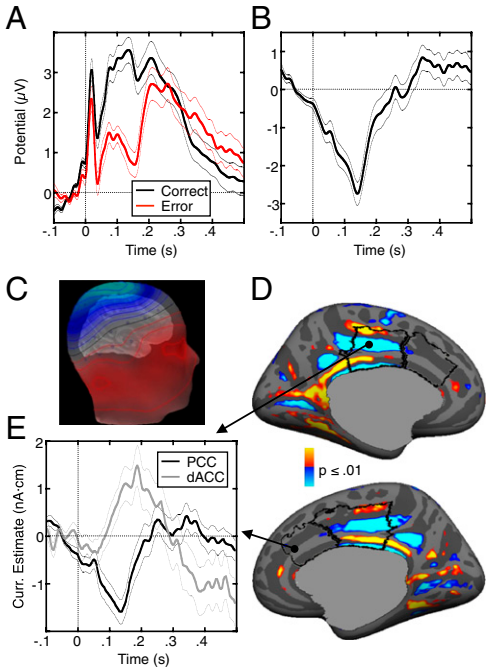

Fig. 2. ERN. (*A*) Grand average waveforms for correct (black) and error (red) trials, time-locked to the onset of the saccade. (*B*) Difference waveform, obtained by subtracting the correct waveform from the error waveform. (*C*) Scalp distribution of the grand average EEG potentials at the time of the peak in the difference waveform displayed on the template head. Blue and red indicate negative and positive values, respectively. (*D*) Combined MEG/EEG source estimate of the ERN displayed on the inflated medial cortical surfaces. The statistical maps show vertices where the current estimate was significantly different from zero. The dACC and dorsal PCC are outlined in black. Positive (red) and negative (blue) values indicate currents flowing out and into the cortex, respectively. (*E*) Time course of the current estimate at the vertices with maximum significance (black circles) in the PCC (black line) and dACC (gray line) at the time of the ERN peak. In *A*, *B*, and *E*, the thin lines on either side of the waveforms represent the SEM for each time sample.

ERN. ***ERN waveforms.*** The ERN was observed as a robust negative deflection in the difference waveform for error vs. correct trials that peaked 138 ms following the response (Fig. 2 *A* and *B*). The average potential between 0 and 200 ms postresponse was significantly lower for error than correct trials [$t(29) = 9.82$, $P < 10^{-10}$]. The average peak amplitude of the ERN across participants was 3.58 ± 1.77 μV, and its latency was 138 ± 26 ms. As in prior antisaccade studies (26, 27), both the correct and error waveforms were superimposed on a slow positive signal; consequently, the peak of the error waveform was positive. In the subtraction, this slow signal cancelled out and the scalp distribution of the ERN difference wave had a single negative peak at electrode Cz (Fig. 2*C*), consistent with some previous reports (Table S1). This suggests a radial source in the posterior medial wall. We also observed an error-related positivity (Pe) beginning ~300 ms postresponse.

Combined EEG/MEG ERN source localization. The estimated current sources of the ERN were maximally significant in the dorsal region of the PCC bilaterally (Brodmann's area 23/31; Fig. 2 *D* and *E* and Table S2), and the maximal vertex was in Brodmann's area 31 of the left hemisphere. Because the currents were constrained to be normal to the cortex, the corresponding prominent current direction is vertical and oriented downward, consistent with a negative difference potential measured on the scalp (3). In Fig. 2*E*, we show the source waveforms at the vertices within the dACC and PCC showing maximally significant activity at the time of peak ERN on the scalp. The PCC waveform peaked significantly earlier than the dACC waveform (138 vs. 188 ms; $P = 0.04$; *SI Methods*), and only PCC activity reflects the ERN in terms of timing and polarity.

Error-Related fMRI Activation. As expected, there was significantly greater fMRI activation in bilateral dACC for error compared with correct trials (Fig. 3 and Table S3). The PCC showed subthreshold activation. A region of interest (ROI) analysis revealed that activation was significantly greater in the dACC than the dorsal PCC in both hemispheres [left: $t(29) = 2.29$, $P = 0.03$; right: $t(29) = 3.21$, $P = 0.003$].

Relations of ERN, dACC Activation, and Error Rate. ERN amplitude correlated with error-related fMRI activation in bilateral PCC, extending into the precuneus (Fig. 4 and Table S3). The PCC clusters were posterior to and did not include the maximal ERN source vertex in either hemisphere, but they did overlap with PCC vertices showing significant ERN source activity. The lack of exact correspondence may reflect the different nature of fMRI and EEG/MEG signals (reviewed in ref. 30). Although dACC activity did not correlate significantly with ERN amplitude on the cortical surface, ROI analysis showed significant relations in bilateral dACC and right dorsal PCC (Fig. 4). The magnitude of these relations did not differ significantly by region in either hemisphere [left: $t(26) = 0.39$, $P = 0.70$; right: $t(26) = 0.49$, $P = 0.63$]. Error rate was inversely correlated with ERN amplitude [$r(28) = -0.58$, $P = 0.0006$] and with error-related activation in bilateral insula (Table S3). There were no significant effects of age or head coil in these regressions.

Functional Connectivity of the dACC Region Showing Error-Related fMRI Activation. To evaluate whether the dACC and PCC showed coordinated activation, we conducted functional connectivity analyses, with a seed centered on the dACC voxel with maximal error-related activation in each hemisphere (Fig. 3). Activation in the left and right dACC seeds correlated with activation along the medial wall bilaterally, including the PCC regions that were the estimated sources of the ERN (Fig. 5*A* and Table S4). This finding was replicated in a functional connectivity analyses of "resting state" fMRI data from a public database (Fig. S2), in-

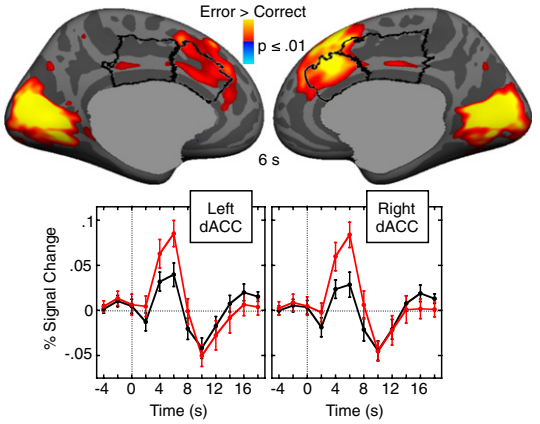

Fig. 3. Error-related fMRI activation at 6 s. Statistical maps are displayed on the inflated medial cortical surfaces. The dACC and dorsal PCC are outlined in black. Warm colors indicate stronger activation on error trials than on correct trials. The gray masks cover subcortical regions in which activity is displaced in a surface rendering. The graphs show the time course of the hemodynamic response in the left and right dACC for error (red) and correct (black) trials averaged across all vertices within the dACC ROIs. Error bars represent the SEM for each time point.

dicating that dACC/PCC connectivity is not unique to the present sample or task.

White Matter Structural Integrity Along the Cingulum Bundle. We hypothesized that if the PCC generates the ERN and relays error information to the dACC to adjust behavior, the speed of self-correction might depend on the myelination of the white matter tracts in the cingulum bundle that connects these two regions. This hypothesis rests on the well-established relation between myelination and conduction velocity (31, 32). To test this, we used DTI to measure fractional anisotropy (FA), which reflects myelination and other white matter properties. Higher FA values in the posterior cingulum bundle predicted faster self-correction on error trials (Fig. 5*B*; Talairach coordinates: $x = 6$, $y = -33$, $z = 35$; Brodmann's area 31, cluster size = 3,168 mm^3, cluster-wise probability value = 0.002).

Supplemental and Control Analyses. ***Simulations of scalp distributions from dACC and PCC sources.*** We conducted forward simulations of potential patterns arising from activation of bilateral (*a*) dACC and (*b*) PCC. These regions correspond to the maxima of error-related fMRI dACC activation and of the estimated ERN source within the PCC. The observed scalp potential pattern was compatible with the simulation for the PCC source but not with the simulated pattern for the dACC source, which peaked 5 cm anterior to the observed peak (Fig. S3).

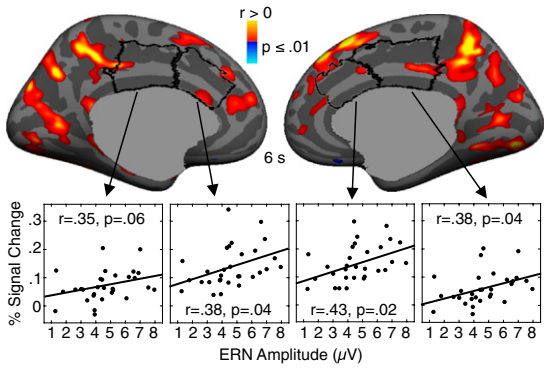

Fig. 4. Relations between error-related fMRI activation and ERN amplitude. Statistical maps showing regression of error-related fMRI activation on ERN amplitude, adjusted for age, are displayed on the inflated medial cortical surfaces. The dACC and dorsal PCC are outlined in black. Warm and cool colors indicate positive and negative correlations, respectively. Scatter plots show fMRI activation in the dACC and dorsal PCC ROIs against ERN amplitude.

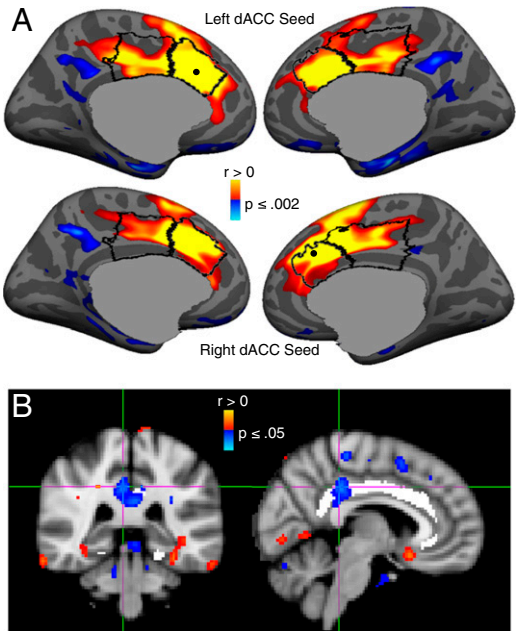

Fig. 5. (*A*) Functional connectivity of the dACC. The statistical maps are projected onto the cortical surface of the template brain. The dACC and dorsal PCC are outlined in black, and the centers of the seed regions are shown as black dots. Activation in both the left (*Upper*) and right (*Lower*) dACC seeds correlated with activation in the dorsal PCC. Warm and cool colors indicate positive and negative correlations, respectively. (*B*) Relation between white matter microstructural integrity as measured by FA in the cingulum bundle and the latency of error self-correction. Images show the statistical map of the correlation. Coronal and sagittal views of the voxel of maximal significance. The cingulum bundle is highlighted in white.

Contribution of saccadic artifact to the ERN. As in prior antisaccade studies (see figure 3 of ref. 26), the horizontal electrooculogram (EOG) signals for saccades to the left and right were of almost identical amplitude but of opposite polarity (Fig. S4*A*). Because there were an equal number of stimuli to the right and left and errors to the right and left were almost equally likely based on a comparison of individual error rates [left: 19 ± 12%, right: 18 ± 11%; $t(29) = 0.25$, $P = 0.81$], the effects of horizontal eye movements are effectively eliminated when the waveforms for correct and error trials are averaged. The remaining saccadic artifact peaks at 19 ms (Fig. 2*A*) and consists of a positive deflection that returns almost to its baseline (i.e., value at time 0) about 100 ms before the peak of the ERN and is common to left and right saccades. It is mostly eliminated when the correct and error waveforms are subtracted to derive the ERN. Thus, artifact from the initial saccade cannot account for the ERN, and artifact from the corrective saccade is not likely to contribute to the ERN. Corrective saccades are jittered in time relative to the error, which reduces their effect, and, on average, they are initiated 41 ms after the peak ERN (Fig. S4 *B* and *C*).

Discussion

The present findings challenge the theory that the ERN and error-related fMRI activation of the dACC reflect the same underlying neural mechanism. Participants showed both a robust ERN and significant error-related fMRI activation of the dACC.

However, the combined MEG and EEG data localized the source of the ERN to the PCC (Brodmann's area 23/31). Importantly, this region was clearly distinct from the dACC region showing error-related activation in fMRI in the same participants performing the same task. This finding is consistent with evidence from prior studies that ERN source locations are posterior to the mean locus of error-related fMRI activation (Fig. 1). ERN amplitude correlated with fMRI activation of both the dACC and PCC and these two regions showed coordinated activity based on functional connectivity MRI. Finally, the microstructural integrity of the white matter underlying the PCC predicted faster self-correction on error trials. Taken together, these findings suggest that the ERN is generated by the PCC, which coordinates with the dACC to recognize errors and adjust responses.

Methodological differences may account for why we observed a PCC source for the ERN, whereas many prior studies reported a source in the dACC. We combined simultaneously acquired MEG and EEG data, which can give a more accurate source localization than either modality alone because of their different biophysical characteristics (33). In addition, our source model is based on individual cortical geometry from structural MRI and assumes that the principal orientation of the currents is normal to the cortex. Using this model and simulations of a source in either the PCC or dACC, we confirmed that the observed scalp distribution at the time of the peak ERN is compatible with activity in the PCC and clearly discordant with activity in the dACC. Our ERN scalp distribution was maximal at electrode Cz, as was the case in many prior studies (Table S1), some of which have reported a dipole source in the dACC rather than the PCC (34, 35). The anterior location of the dipole is most likely attributable to the fact that the equivalent dipoles in those studies were oriented at an acute angle relative to the cortical mantle. Using a forward simulation, we demonstrated that a slanted dipole in the dACC can produce a scalp distribution similar to that of the present study (Fig. S3*D*). Our model excluded the possibility of a slanted dipole by assuming that the currents are oriented normal to the cortex. This assumption is valid because ERPs arise from postsynaptic currents in the apical dendrites of pyramidal neurons, which guide the current to be oriented perpendicular to the cortical surface (36, 37).

Another concern is whether the observed ERN is the canonical ERN described in the literature. The ERN is thought to represent a "generic" error marker that is present for errors in a wide range of contexts (3). It is elicited by errors committed with the feet (38), eyes, and hands in a variety of tasks. A prior study that compared ERNs generated by button presses and saccades found them to be similar in morphology, amplitude, and scalp topography (39). Because we only studied antisaccades, we cannot exclude the possibility that ERN generation differs as a function of movement modality or task requirements. Nonetheless, a comparison of our ERN with those described in the literature with regard to scalp distribution (see above), latency, and morphology suggests that our ERN is compatible with the generic ERN of the literature.

With regard to latency, the vast majority of ERN studies are time-locked to button presses, which elicit markedly shorter ERN latencies than EMG-locked ERNs (Table S1). This likely reflects that EMG measures the onset of movement, which occurs earlier than the button press. Our ERN was also time-locked to movement onset, in this case, a saccade, based on EOG, and our ERN latency (138 ms) is in the range of EMG-locked ERNs (Table S1, range: 83–165 ms). Our ERN latency is slightly longer than those of prior antisaccade studies (Table S1, range: 80–130 ms), several of which used a "precue" that may have allowed an earlier initiation of movement planning and ERN generation (26, 28, 29).

With regard to morphology, many prior ERN studies have shown a more robust Pe. The Pe has been linked to error awareness (40), and, consistent with this, in prior antisaccade studies, the magnitude of the Pe has depended on whether or not the error was perceived. The Pe was weak in one study (27), stronger for perceived errors in another study (28), and only present for perceived errors in two studies (26, 29). Although we did not ask participants to indicate error awareness, based on the finding that perceived antisaccade errors have longer self-correction latencies (26, 28, 29), we divided error trials for each participant based on the median self-correction latency. We found a more robust Pe for error trials with longer self-correction latencies (Fig. S5), which are more likely to be perceived errors.

Although MEG/EEG detected error-related activity in the PCC but not in the dACC, fMRI showed significant error-related activity in the dACC but not in the PCC. Because we lack invasive physiological data that would allow us to reconcile these differences, we can only speculate about their bases in terms of the different sources of signals in these techniques. Because MEG and EEG signals reflect the net effect of the vectorial electrical currents within a region, there will be cancellation attributable to opposing orientations of currents if there is (*a*) bilaterally symmetrical activity in gyri on the medial surface or (*b*) activity on opposite banks of a sulcus (41). Our fMRI data indicate that error-related activity extends to opposite walls of the dorsal anterior cingulate sulcus, which may have led to cancellation in both EEG and MEG. Although we cannot definitively exclude the possibility that cortical currents in the dACC exhibit an ERN time course, the absence of a dACC source corresponding to the ERN and the strong source within the PCC are more consistent with a PCC source of the ERN. A PCC source is also consistent with several prior ERN studies (Fig. 1), a recent MEG report of a PCC source for the feedback-related negativity (24), and a prior DTI finding that ERN amplitude correlates with FA in the posterior cingulum bundle (a finding we did not replicate here) (42). Although several prior fMRI studies have shown error-related activation in both the PCC and dACC (18, 19), in the present study, the activation seen in bilateral PCC (Fig. 3) did not survive correction for multiple comparisons. The absence of strong PCC activation in most fMRI studies of error processing may reflect the mechanism of ERN generation. The ERN has been theorized to arise from disinhibition of cortical neurons by dopaminergic midbrain neurons (3), which might not lead to an increase in the blood oxygen level-dependent signal (43). Another possibility is that the ERN arises as a result of synchronization of constantly active but otherwise asynchronous neural populations. This would make a difference in the MEG/EEG signals but not necessarily in hemodynamic activity.

Our multimodal neuroimaging data suggest that the dACC and PCC work together to mediate error processing. Functional connectivity analyses showing coordinated fMRI activation in the PCC and dACC both during our task and during rest support the hypothesis that these regions are components of a functional network. The PCC and ACC have direct anatomical connections through the cingulum bundle (44). Our ERN localization lies within the dorsal PCC, which is connected to the dACC, whereas the ventral PCC is connected to the rostral ACC and other "default network" regions (45). One possible interpretation of our findings is that the PCC detects errors, gives rise to the ERN, and then relays error information to the dACC via the cingulum bundle to implement corrective behavior. This proposal is consistent with our DTI finding that increased FA in the posterior cingulum bundle predicts faster self-correction on error trials. To the degree that FA reflects myelination, increased FA may speed the conduction of the message that an error has occurred and corrections need to be initiated. This proposal also jibes with human neuroimaging, lesion, and neurophysiology evidence that rather than playing a specific role in error detection, the dACC is involved in within-trial behavioral adjustment (46–48). Our findings are also relevant to understanding other dissociations between the ERN and fMRI activation of the dACC. These

include findings of increased dACC activation on high-conflict correct trials in the absence of an ERN (15). This may reflect that although the ERN specifically signals an error, dACC activation indexes a more general need for increased cognitive control, including the need for behavioral adjustment following errors.

In summary, we present evidence from complementary neuroimaging techniques that the PCC is the generator of the ERN and that it is functionally related to the dACC. More research is necessary to understand the interplay between the PCC and dACC during error commission, why hemodynamic and electrophysiological techniques are differentially sensitive to error-related activity in these regions, and whether the present findings generalize beyond antisaccade tasks.

Methods

Participants. Of the 44 healthy participants who enrolled, 30 (10 female, aged 36 ± 13 y) successfully completed both the EEG/MEG and fMRI sessions and made a sufficient number of errors to be included in the functional analyses (minimum of 20 for EEG/MEG and 10 for fMRI). Forty-two (15 female, aged 35 ± 13 y) made enough errors (n = 5) to be included in the regression of DTI data on self-correction latency, which was based on EOG data. All participants gave written informed consent, and the study was approved by the Partners Human Research Committee.

Antisaccade Paradigm. The task consisted of a pseudorandom sequence of three types of antisaccade trials and fixation epochs (Fig. S1 and *SI Methods*). Participants were instructed to respond as quickly and accurately as possible by making a saccade away from the stimulus. Trials with initial saccades in the direction of the stimulus were scored as errors.

Recording and Scoring of Eye Movement Data. The ISCAN fMRI Remote Eye Tracking Laboratory (Burlington, MA) recorded eye position during mock and fMRI scanning using a 120-Hz video camera. In MEG/EEG, the horizontal and vertical components of eye movements were recorded using two pairs of bipolar EOG electrodes. Eye movement data were scored offline using a partially automated program (*SI Methods*).

Error rates were logit-transformed before analysis to normalize their distribution. Saccadic latency was analyzed with repeated-measures ANOVA with factors for modality (fMRI, EEG/MEG) and trial type (correct, error).

MRI Acquisition. Images were acquired with a 3.0-T Siemens Trio whole-body high-speed imaging device equipped for echo planar imaging (Siemens Medical Systems). For each participant, we acquired two structural scans (T1), six functional scans (T2), a fast low-angle shot (FLASH) scan for construction of the boundary-element model for MEG/EEG source analysis, and a DTI scan. Scan parameters are presented in *SI Methods*.

Simultaneous EEG and MEG Acquisition. MEG data were acquired in a magnetically shielded room (IMEDCO) using a dc-SQUID Neuromag VectorView system (Elekta–Neuromag) comprising 306 sensors arranged in triplets of two orthogonal planar gradiometers and a magnetometer distributed at 102 locations around the entire scalp. EEG data were acquired simultaneously using a 70-channel electrode cap. EEG electrode impedances were brought below 20 kiloOhms at the start of each recording session. All signals were identically filtered a bandpass of 0.1–200 Hz and digitized at 600 Hz.

To allow registration of EEG/MEG and MRI data and to record head position relative to the sensor array, the locations of three fiduciary points (nasion and auricular points) defining a head-based coordinate system, the sites of four head position indicator (HPI) coils, and a set of points from the head surface were digitized using a 3Space Fastrak digitizer (Polhemus) integrated with the VectorView system. At the beginning of each MEG acquisition, currents were fed to the HPI coils and their magnetic fields were used to calculate the relative location of the head with respect to the MEG sensor array.

Surface-Based Analyses for fMRI and EEG/MEG Source Localization. Detailed information is provided in *SI Methods*. Analyses were conducted on each participant's cortical surface, which was reconstructed using FreeSurfer (http://surfer.nmr.mgh.harvard.edu). Individual cortical surfaces were registered to a template brain by optimally aligning individual sulcal-gyral patterns. Cortical activation was localized using automated surface-based parcellation software (49). For ROI analyses, the dACC and dorsal PCC were defined in each hemisphere using anatomical landmarks (*SI Methods*). Activation was quantified by averaging across the vertices in each ROI.

Preprocessing of EEG and MEG Data. Detailed information is provided in *SI Methods*. After excluding noisy EEG channels, EEG data were referenced to the grand average. MEG channels were processed using the signal-space separation method (50). MEG/EEG data were low-pass-filtered at 40 Hz, and trials with eye blinks were excluded. Response-locked data were baseline-corrected, and correct and error trials were averaged separately for each participant.

Identification of the ERN. The ERN was derived using the average signal across the following 10-20 electrode locations: FC1, FCz, FC2, C1, Cz, C2, CP1, CPz, and CP2 for each participant. On average, seven of these nine channels produced usable data. The ERN was based on an average of 328 ± 85 correct trials and 60 ± 29 error trials per participant. The peak ERN for the group was identified within the 200 ms following saccadic initiation as the point of maximal difference for the error vs. correct waveforms. The peak ERN for each participant was identified as the point of maximal difference within 50 ms on either side of the group peak.

Combined EEG/MEG ERN Source Localization. MNE software (www.martinos.org/martinos/userInfo/data/sofMNE.php) was used to derive current source estimates of the difference waveform (error-correct) from the combined EEG and MEG group data. The reconstructed cortical surfaces for each participant, which comprised ~100,000 vertices per hemisphere, were decimated to a subset of ~3,000 dipole locations (vertices) per hemisphere. The forward solution was calculated using a three-compartment boundary-element model (36), with the inner and outer skull surfaces and the scalp surface segmented from the FLASH images. The head position information from the start of each run was used in the calculation of a forward solution for all runs, which were averaged together. The amplitudes of the dipoles at each cortical location were estimated every 4 ms using the anatomically constrained linear estimation approach (51). The orientations of the dipoles were tightly constrained to the cortical normal direction by setting source variances for the transverse current components to be 0.1 times the variance of the currents normal to the cortical surface (52). Individual source estimate data were mapped to the template cortical surface. This resulted in a set of source estimates at each time point that were spatially aligned across participants.

To localize the ERN source, we used the source estimate of the difference waveform at the time of the peak ERN for each participant. We used a t test to determine whether the averaged amplitudes of the source estimates differed from zero at each vertex on the cortical surface. Correction for multiple comparisons was based on a permutation analysis (*SI Methods*).

Source Simulations. Using the cortical geometry of the template brain and a three-compartment boundary element model, we conducted forward solutions for dipoles in the maximum vertex of (*a*) the estimated ERN source in the PCC and (*b*) error-related fMRI activation in the dACC. These simulations assumed a current direction normal to the cortical mantle.

Analysis of fMRI Data. Detailed information is provided in *SI Methods*. fMRI analyses were conducted using FreeSurfer Functional Analysis Stream software. We compared activation on error vs. correct trials at 6 s on the cortical surface. We also compared the magnitude of error-related activation in bilateral dACC and PCC ROIs. For all surface-based fMRI analyses, Monte Carlo simulations were the basis of correction for multiple comparisons.

Relations of ERN, dACC Activation, and Error Rate. Both ERN amplitude and error-related fMRI activation were regressed on error rate. We also regressed error-related fMRI activation on ERN amplitude. Because age correlates with both the ERN (34) and error-related activation in medial prefrontal cortex (11), age was included as a covariate in these analyses. In addition, for regressions involving fMRI activation, head coil (12 or 32 channels) was also included as a covariate. To determine whether the magnitude of the relations of dACC and PCC fMRI activation with ERN amplitude differed significantly, we fit a regression model with ERN as the response and fMRI activation in the dACC and PCC ROIs in each hemisphere as covariates. We then used t tests to compare the slopes for the two regions in each hemisphere.

Functional Connectivity MRI Analysis. Seed-based functional connectivity analyses were conducted on the fMRI data from the present study and from the resting state data of 45 participants in a public database (www.nitrc.org/projects/fcon_1000). These analyses were conducted in the volume and used a false discovery rate threshold of $P \leq 0.01$ to determine significance. The methods are detailed in a previous report (53) and in *SI Methods*. The seeds

were spheres with a 4-mm radius, which were centered on the dACC vertex with the maximum error-related fMRI activation at the 6-s timepoint in each hemisphere. The resulting statistical maps were projected onto the cortical surface for visualization.

DTI Analysis. To examine the relations of white matter microstructural integrity with the latency of corrective behavior on error trials, we regressed the average latencies of corrective saccades with FA values along the cingulum bundle using age as a covariate (*SI Methods*).

ACKNOWLEDGMENTS. We thank Randy Buckner, Hesheng Liu, and Mark Vangel for consultation. Support for this study was provided by National Institute for Mental Health Grants F32 MH088081 (to Y.A.), F32 MH082514 (to K.A.D.), 1R21MH084041-01A1 (to N.M.) and R01 MH67720 (to D.S.M.); National Institute on Drug Abuse Grant 1R01DA027804-01 (to N.M.); the Massachusetts General Hospital Fund for Medical Discovery (to Y.A.); National Center for Research Resources Grant P41 RR014075-11 (to M.S.H.); National Institute of Biomedical Imaging and Bioengineering Grant 5R01EB009048 (to M.S.H.); and the American Recovery and Reinvestment Act (ARRA) - National Center for Complementary and Alternative Medicine (NCCAM) (to N.M.).

1. Taylor SF, Stern ER, Gehring WJ (2007) Neural systems for error monitoring: Recent findings and theoretical perspectives. *Neuroscientist* 13:160–172.
2. Keil J, Weisz N, Paul-Jordanov I, Wienbruch C (2010) Localization of the magnetic equivalent of the ERN and induced oscillatory brain activity. *Neuroimage* 51:404–411.
3. Holroyd CB, Coles MG (2002) The neural basis of human error processing: Reinforcement learning, dopamine, and the error-related negativity. *Psychol Rev* 109: 679–709.
4. Ridderinkhof KR, Ullsperger M, Crone EA, Nieuwenhuis S (2004) The role of the medial frontal cortex in cognitive control. *Science* 306:443–447.
5. Gehring WJ, Goss B, Coles MG, Meyer DE, Donchin E (1993) A neural system for error detection and compensation. *Psychol Sci* 4:385–390.
6. Scheffers MK, Coles MG (2000) Performance monitoring in a confusing world: Error-related brain activity, judgments of response accuracy, and types of errors. *J Exp Psychol Hum Percept Perform* 26:141–151.
7. Holroyd CB, Larsen JT, Cohen JD (2004) Context dependence of the event-related brain potential associated with reward and punishment. *Psychophysiology* 41: 245–253.
8. Debener S, et al. (2005) Trial-by-trial coupling of concurrent electroencephalogram and functional magnetic resonance imaging identifies the dynamics of performance monitoring. *J Neurosci* 25:11730–11737.
9. Fiehler K, Ullsperger M, von Cramon DY (2005) Electrophysiological correlates of error correction. *Psychophysiology* 42:72–82.
10. Polli FE, et al. (2008) Reduced error-related activation in two anterior cingulate circuits is related to impaired performance in schizophrenia. *Brain* 131:971–986.
11. Fitzgerald KD, et al. (2010) The development of performance-monitoring function in the posterior medial frontal cortex. *Neuroimage* 49:3463–3473.
12. Kerns JG, et al. (2004) Anterior cingulate conflict monitoring and adjustments in control. *Science* 303:1023–1026.
13. Garavan H, Ross TJ, Murphy K, Roche RA, Stein EA (2002) Dissociable executive functions in the dynamic control of behavior: Inhibition, error detection, and correction. *Neuroimage* 17:1820–1829.
14. Klein TA, et al. (2007) Neural correlates of error awareness. *Neuroimage* 34: 1774–1781.
15. Ullsperger M, von Cramon DY (2001) Subprocesses of performance monitoring: A dissociation of error processing and response competition revealed by event-related fMRI and ERPs. *Neuroimage* 14:1387–1401.
16. Mathalon DH, Whitfield SL, Ford JM (2003) Anatomy of an error: ERP and fMRI. *Biol Psychol* 64:119–141.
17. Bush G, Luu P, Posner MI (2000) Cognitive and emotional influences in anterior cingulate cortex. *Trends Cogn Sci* 4:215–222.
18. Fassbender C, et al. (2004) A topography of executive functions and their interactions revealed by functional magnetic resonance imaging. *Brain Res Cogn Brain Res* 20: 132–143.
19. Wittfoth M, Küstermann E, Fahle M, Herrmann M (2008) The influence of response conflict on error processing: Evidence from event-related fMRI. *Brain Res* 1194: 118–129.
20. Menon V, Adleman NE, White CD, Glover GH, Reiss AL (2001) Error-related brain activation during a Go/NoGo response inhibition task. *Hum Brain Mapp* 12:131–143.
21. Fujiwara J, Tobler PN, Taira M, Iijima T, Tsutsui K (2009) Segregated and integrated coding of reward and punishment in the cingulate cortex. *J Neurophysiol* 101: 3284–3293.
22. McCoy AN, Crowley JC, Haghighian G, Dean HL, Platt ML (2003) Saccade reward signals in posterior cingulate cortex. *Neuron* 40:1031–1040.
23. Smith BW, et al. (2009) Neural substrates of reward magnitude, probability, and risk during a wheel of fortune decision-making task. *Neuroimage* 44:600–609.
24. Doñamayor N, Marco-Pallarés J, Heldmann M, Schoenfeld MA, Münte TF (2011) Temporal dynamics of reward processing revealed by magnetoencephalography. *Hum Brain Mapp*, in press.
25. Polli FE, et al. (2005) Rostral and dorsal anterior cingulate cortex make dissociable contributions during antisaccade error commission. *Proc Natl Acad Sci USA* 102: 15700–15705.
26. Nieuwenhuis S, Ridderinkhof KR, Blom J, Band GP, Kok A (2001) Error-related brain potentials are differentially related to awareness of response errors: Evidence from an antisaccade task. *Psychophysiology* 38:752–760.
27. Belopolsky AV, Kramer AF (2006) Error-processing of oculomotor capture. *Brain Res* 1081:171–178.
28. Wessel JR, Danielmeier C, Ullsperger M (2011) Error awareness revisited: Accumulation of multimodal evidence from central and autonomic nervous systems. *J Cogn Neurosci* 23:3021–3036.
29. Endrass T, Reuter B, Kathmann N (2007) ERP correlates of conscious error recognition: Aware and unaware errors in an antisaccade task. *Eur J Neurosci* 26:1714–1720.
30. Ritter P, Villringer A (2006) Simultaneous EEG-fMRI. *Neurosci Biobehav Rev* 30: 823–838.
31. Waxman SG (1980) Determinants of conduction velocity in myelinated nerve fibers. *Muscle Nerve* 3:141–150.
32. Stufflebeam SM, et al. (2008) A non-invasive method to relate the timing of neural activity to white matter microstructural integrity. *Neuroimage* 42:710–716.
33. Sharon D, Hämäläinen MS, Tootell RB, Halgren E, Belliveau JW (2007) The advantage of combining MEG and EEG: Comparison to fMRI in focally stimulated visual cortex. *Neuroimage* 36:1225–1235.
34. Ladouceur CD, Dahl RE, Carter CS (2007) Development of action monitoring through adolescence into adulthood: ERP and source localization. *Dev Sci* 10:874–891.
35. Alain C, McNeely HE, He Y, Christensen BK, West R (2002) Neurophysiological evidence of error-monitoring deficits in patients with schizophrenia. *Cereb Cortex* 12: 840–846.
36. Hämäläinen MS, Hari R, Ilmoniemi R, Knuutila J, Lounasmaa O (1993) Magnetoencephalography—Theory, instrumentation, and applications to noninvasive studies of the working human brain. *Rev Mod Phys* 65:413–497.
37. Luck SJ (2005) *An Introduction to the Event-Related Potential Technique* (MIT Press, Cambridge, MA).
38. Holroyd CB, Dien J, Coles MG (1998) Error-related scalp potentials elicited by hand and foot movements: Evidence for an output-independent error-processing system in humans. *Neurosci Lett* 242:65–68.
39. Van't Ent D, Apkarian P (1999) Motoric response inhibition in finger movement and saccadic eye movement: A comparative study. *Clin Neurophysiol* 110:1058–1072.
40. Overbeek TJM, Nieuwenhuis S, Ridderinkhof KR (2005) Dissociable components of error processing. *J Psychophysiol* 19:319–329.
41. Ahlfors SP, et al. (2010) Cancellation of EEG and MEG signals generated by extended and distributed sources. *Hum Brain Mapp* 31:140–149.
42. Westlye LT, Walhovd KB, Bjørnerud A, Due-Tønnessen P, Fjell AM (2009) Error-related negativity is mediated by fractional anisotropy in the posterior cingulate gyrus—A study combining diffusion tensor imaging and electrophysiology in healthy adults. *Cereb Cortex* 19:293–304.
43. Logothetis NK (2008) What we can do and what we cannot do with fMRI. *Nature* 453: 869–878.
44. Schmahmann JD, et al. (2007) Association fibre pathways of the brain: Parallel observations from diffusion spectrum imaging and autoradiography. *Brain* 130:630–653.
45. Vogt BA, Vogt L, Laureys S (2006) Cytology and functionally correlated circuits of human posterior cingulate areas. *Neuroimage* 29:452–466.
46. Magno E, Foxe JJ, Molholm S, Robertson IH, Garavan H (2006) The anterior cingulate and error avoidance. *J Neurosci* 26:4769–4773.
47. Modirrousta M, Fellows LK (2008) Dorsal medial prefrontal cortex plays a necessary role in rapid error prediction in humans. *J Neurosci* 28:14000–14005.
48. Williams ZM, Bush G, Rauch SL, Cosgrove GR, Eskandar EN (2004) Human anterior cingulate neurons and the integration of monetary reward with motor responses. *Nat Neurosci* 7:1370–1375.
49. Fischl B, et al. (2004) Automatically parcellating the human cerebral cortex. *Cereb Cortex* 14:11–22.
50. Taulu S, Kajola M (2005) Presentation of electromagnetic multichannel data: The signal space separation method. *J Appl Phys* 97(124905):1–10.
51. Hämäläinen MS, Ilmoniemi R (1984) Interpreting measured magnetic fields of the brain: Estimates of current distribution. (University of Technology, Department of Technical Physics Report, Helsinki), p TKK-F-A559.
52. Lin FH, Belliveau JW, Dale AM, Hämäläinen MS (2006) Distributed current estimates using cortical orientation constraints. *Hum Brain Mapp* 27:1–13.
53. Tu P, Buckner RL, Zollei L, Dyckman KA, Manoach DS (2010) Reduced functional connectivity in a right-hemisphere network for volitional ocular motor control in schizophrenia. *Brain* 133:625–637.
54. Desikan RS, et al. (2006) An automated labeling system for subdividing the human cerebral cortex on MRI scans into gyral based regions of interest. *Neuroimage* 31: 968–980.